Geophysical Journal International

Geophys. J. Int. (2022) **231,** 2173–2185
Advance Access publication 2022 August 17
GJI Seismology

https://doi.org/10.1093/gji/ggac323

Frequency-difference backprojection of earthquakes

Jing Ci Neo [1], Wenyuan Fan [2], Yihe Huang[1] and David Dowling[3]

[1] *Department of Earth and Environmental Sciences, University of Michigan, Ann Arbor, MI 48109, USA. E-mail: neoj@umich.edu*
[2] *Scripps Institution of Oceanography, UC San Diego, La Jolla, CA 92037, USA*
[3] *Department of Naval Architecture and Marine Engineering, University of Michigan, Ann Arbor, MI 48109-2145, USA*

Accepted 2022 August 10. Received 2022 August 8; in original form 2022 January 19

SUMMARY

Backprojection has proven useful in imaging large earthquake rupture processes. The method is generally robust and requires relatively simple assumptions about the fault geometry or the Earth velocity model. It can be applied in both the time and frequency domain. Backprojection images are often obtained from records filtered in a narrow frequency band, limiting its ability to uncover the whole rupture process. Here, we develop and apply a novel frequency-difference backprojection (FDBP) technique to image large earthquakes, which imitates frequencies below the bandwidth of the signal. The new approach originates from frequency-difference beamforming, which was initially designed to locate acoustic sources. Our method stacks the phase-difference of frequency pairs, given by the autoproduct, and is less affected by scattering and -time errors from 3-D Earth structures. It can potentially locate sources more accurately, albeit with lower resolution. In this study, we first develop the FDBP algorithm and then validate it by performing synthetic tests. We further compare two stacking techniques of the FDBP method, Band Width Averaged Autoproduct and its counterpart (BWAP and non-BWAP), and their effects in the backprojection images. We then apply both the FDBP and conventional backprojection methods to the 2015 *M*7.8 Gorkha earthquake as a case study. The backprojection results from the two methods agree well with each other, and we find that the peak radiation loci of the FDBP non-BWAP snapshots have standard error of less than 0.33° during the rupture process. The FDBP method shows promise in resolving complex earthquake rupture processes in tectonically complex regions.

Key words: Time-series analysis; Body waves; Computational seismology; Earthquake source observations; Wave propagation.

1 INTRODUCTION

Understanding earthquake rupture processes is fundamental to studying earthquake physics and estimating seismic hazards. However, large earthquakes often rupture in complex ways, which are challenging to resolve via traditional means. Backprojection is an imaging technique to study earthquake rupture evolution (Ishii *et al.* 2005; Krüger & Ohrnberger 2005). The method is data driven and computationally efficient; thus, it has potential in hazard warning applications (e.g. Hayes *et al.* 2011). Uniquely, backprojection can take advantage of coherent high-frequency seismic body waves to discern earthquake rupture velocity and relative location of seismic radiation sources while making few assumptions about the fault geometry (see summary in Kiser & Ishii 2017). Hence, backprojection results have led to improved understanding of the inter-relations between rupture propagation, fault geometry, surrounding material lithology and earthquake triggering (e.g. Walker & Shearer 2009; Meng *et al.* 2012b; Okuwaki & Yagi 2018; Fan *et al.* 2019).

Backprojection uses simple *P* waves and takes advantage of source–receiver reciprocity to image earthquakes. The method can be implemented in either the time domain or the frequency domain (e.g. Manchee & Weichert 1968; Goldstein & Archuleta 1987; Ishii *et al.* 2005; Krüger & Ohrnberger 2005; Tan *et al.* 2019), and it has also been applied to various arrays with different configurations (e.g. Xu *et al.* 2009; Wang & Mori 2011; Kiser & Ishii 2012). Although the data processing procedures of different methods can cause some variations (Rost & Thomas 2002; Meng *et al.* 2016; Qin & Yao 2017), the general rupture features are similar (Avouac *et al.* 2015; Yagi & Okuwaki 2015; Zhang *et al.* 2016; Wang & Mori 2016; Liu *et al.* 2017), showing the robustness of the backprojection results. The stability results from stacking coherent waveforms, and the approach does not perform a formal inversion with physical constraints. However, the method can suffer from imaging artefacts when there are coherent signals that are not from the rupture process (e.g. Meng *et al.* 2012a). Such artefacts can be caused by near-source scatters, for example depth phases and

water phases (Yue *et al.* 2017; Fan & Shearer 2018). The backprojection images can also suffer from strong 3-D velocity influences in causing inaccurate traveltime predictions or limited array footprints that can distort the array responses (e.g. Okuwaki *et al.* 2014; Meng *et al.* 2016). Furthermore, complex ruptures may involve multiple distinct faults that have varying focal mechanisms, posing challenges to accurately resolve the spatiotemporal propagation of these earthquakes (e.g. Zeng *et al.* 2020). Mitigating such biases and quantifying the uncertainties remain key issues in backprojection studies.

Here we develop a novel frequency-difference backprojection method (FDBP) aimed to explore the uncertainties in earthquake imaging. The frequency-difference method was first introduced in acoustic beamforming (Abadi *et al.* 2012). It can accurately resolve the arrival of a signal even in the presence of wave propagation effects that cannot be fully characterized by a known velocity model. The basis of this method lies in the inherent trade-off between robustness and resolving power of any given wavelength. Backprojection results of higher frequencies become increasingly unstable as the period of the waves approaches the magnitude of error in predicted traveltimes. To circumvent this limitation, the frequency-difference method uses 'autoproducts' to simulate lower frequencies. The autoproduct is given by the quadratic product of a complex wavefield with the complex conjugate of another wavefield at a different frequency. The phase-difference of each frequency pair mimics the phase of a wave at the difference-frequency (Fig. 1a). Such a procedure can potentially resolve source locations with higher accuracy (Fig. 1b), albeit with lower resolution. Additionally, the autoproducts can be averaged incoherently over a frequency band of interest, which may further reduce the impacts from multipathing or scattering under certain conditions (Worthmann & Dowling 2017).

In this study, we first develop the theoretical and numerical frameworks of using FDBP to image earthquakes, and then apply the method to the 2015 M_w 7.8 Gorkha, Nepal earthquake to investigate its rupture process as a case study. We evaluate the method by performing synthetic tests using both Ricker wavelets and waveforms from two aftershocks of the main shock. Our synthetic tests are benchmarked with results from the conventional time-domain and frequency-domain backprojection methods. We also explore a range of empirical parameters used in the FDBP imaging procedure to examine their effects on the results. In general, our synthetic tests show that FDBP can image seismic radiation accurately, and the method appears less sensitive to noise when compared to conventional backprojection methods. For the 2015 Gorkha earthquake, the rupture characteristics resolved by FDBP are consistent with previous results, especially in a high frequency (0.3–2 Hz) band. Our results indicate that FDBP is a promising new method, and its robust results may provide new insights into complex earthquake rupture processes.

2 THEORY

2.1 Conventional backprojection

Conventional time-domain *P*-wave backprojection aligns the seismic waveforms with their initial arrivals, and then back-propagates the records to a set of grids near the earthquake hypocentre to infer its rupture process. For simplicity, herein the conventional time-domain backprojection is referred to as CTBP for comparison with FDBP. The stacked waveforms from CTBP at a candidate source (grid location $\underline{r}$) is given by

$$B_{\text{conv}}(\underline{r}, t) = \sum_{k=1}^{N} \frac{1}{n_k} d_k(t + \tau_k(\underline{r}) + s_k), \tag{1}$$

where $d_k(t)$ is the velocity record of the kth station at time t, $\underline{r}$ is the source grid location, $\tau_k(\underline{r})$ is the predicted traveltime from $\underline{r}$ to the kth station and s_k is the time correction term obtained from cross-correlation (Section 3.1). The velocity record of each station is inversely weighted by the total number of stations within 5° station, n_k, to enhance the signals recorded at sparsely distributed stations (e.g. Fan & Shearer 2015). Finally, the backprojection energy is computed as the root-mean-square (RMS) of the stacked waveforms over a time window T,

$$E_{\text{conv}}(\underline{r}) = \sqrt{\langle (B_{\text{conv}}(\underline{r}, t))^2 \rangle_T}, \tag{2}$$

where the angle brackets denote an average over T and E represents the backprojection energy.

In the frequency domain, conventional backprojection (referred to as CFBP) selects a time window, shifts the spectra in phase, stacks spectra from different stations, and averages the stacks over the frequency band of interest. The phase-shifts are equivalent to the time-shifts in the time domain. The waveforms are divided into segments to investigate the temporal propagation. Taking the earthquake hypocentre as a reference point ($\underline{r}^0$) for the first time window, the time-shift at grid $\underline{r}$ can be rearranged as

$$\begin{aligned} \tau_k(\underline{r}) &= \tau_k(\underline{r}^0) + [\tau_k(\underline{r}) - \tau_k(\underline{r}^0)] \\ &= \tau_k(\underline{r}^0) + \Delta\tau_k^0(\underline{r}), \end{aligned} \tag{3}$$

where $\tau_k(\underline{r}^0)$ determines the onset of the time window segments and $\Delta\tau_k(\underline{r})$ is used in the phase-shift of the waveforms to obtain the backprojection images. As the rupture moves away from the hypocentre, a Doppler-effect correction is needed to ensure that seismic phases from the same slip episode are included in one time window. Hence, we use the peak energy location of the previous time window as the reference point for the successive time window (e.g. Meng *et al.* 2012a; Wang *et al.* 2016; Yin *et al.* 2018). This method works best for simple rupture cases, such as unilateral, continuous rupture propagations.

Taking $P_k(\omega)$ as the spectrum of the kth station for a time window, where ω is the frequency, the backprojection result at frequency ω is

$$B_{\text{conv}}(\underline{r}, \omega) = \left| \sum_{k=1}^{N} \frac{1}{n_k} P_k(\omega) w_k(\underline{r}, \omega) \right|^2, \tag{4}$$

where $w_k(\underline{r}, \omega) = e^{i\omega\Delta\tau_k^0(\underline{r})}$ is a phase-weighting factor, and the backprojection energy is then calculated by averaging over the frequency range of interest.

$$E_{\text{conv}}(\underline{r}) = \left\langle B_{\text{conv}}(\underline{r}, \omega) \right\rangle_\omega. \tag{5}$$

2.2 Frequency-difference backprojection

When applying the FDBP method, the complex wavefield term in eq. (4) is substituted with the autoproduct, the product of complex wavefields (Douglass & Dowling 2019). The autoproduct simulates a wave at the difference-frequency using the phase difference of a pair of frequencies (Fig. 1a). Assuming that the phase of the source is approximately constant over the frequency band of interest (Worthmann & Dowling 2017) and that arrivals of lower frequency seismic waves can be better predicted, backprojecting the autoproduct can

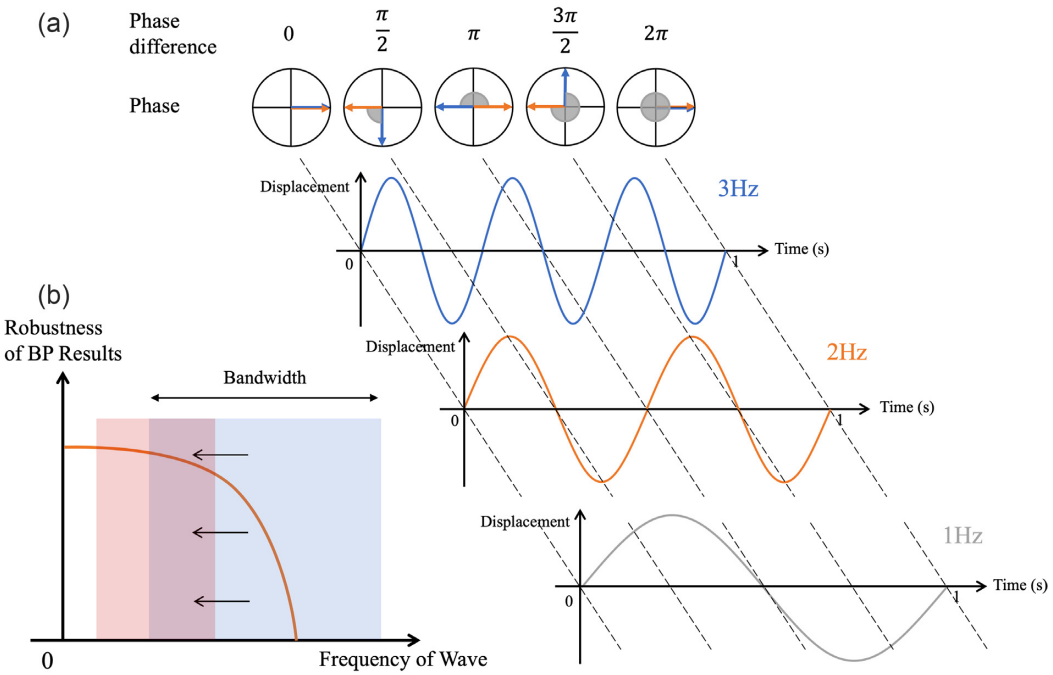

Figure 1. Conceptual sketch of FDBP. (a) Phase difference between two waves (3 and 2 Hz) mimicking the phase of a wave at a difference-frequency (1 Hz). Arrows show the phase of the waves, and the angle indicates the phase difference. (b) Conceptual graph demonstrating FDBP decreases the bandwidth (extent of blue box) to a lower apparent bandwidth (extent of red box), increasing the robustness of the results.

increase the accuracy of the backprojection results (Fig. 1b). The autoproduct, AP_k, measured at the kth station for a pair of frequencies, is defined as:

$$\begin{aligned} AP_k(\bar{\omega}, \Delta\omega) &= P_k(\omega_2)P_k^*(\omega_1) \\ &= P_k\left(\bar{\omega} + \frac{\Delta\omega}{2}\right) P_k^*\left(\bar{\omega} - \frac{\Delta\omega}{2}\right), \end{aligned} \tag{6}$$

where $\bar{\omega}$ is the average and $\Delta\omega$ is the difference of two frequencies, ω_1 and ω_2. Theoretically, smaller values of $\Delta\omega$ would lead to more robust FDBP images.

The autoproduct can then be averaged incoherently (BWAP, band width averaged autoproduct) or coherently (non-BWAP) over the frequency pairs. Here, averaging incoherently (BWAP) means averaging the spectra of the available frequency pairs (complex value) before stacking. Averaging coherently (non-BWAP) means averaging the backprojection results of each pair (real value) after stacking. The incoherently averaged (BWAP) autoproduct is defined as

$$\overline{AP}_k = \langle AP_k(\bar{\omega}, \Delta\omega)\rangle_\omega = \frac{1}{M}\sum_{m=1}^{M} AP_k(\bar{\omega}_m, \Delta\omega) \tag{7}$$

for M sets of average frequencies.

The BWAP procedure can improve the robustness of the results in the presence of random noise, assuming that the phase of the source signal does not change very much over the signal bandwidth such that the autoproduct is coherent for each frequency-pair. It can also mitigate the impact of coherent signal-generated noise in P waves when multiple paths are considered in the Green's function of the backprojection, which would suppress additional terms due to scattered or reflected waves from multiple ray paths (Worthmann *et al.* 2017; Douglass *et al.* 2017; Dowling 2018). It is most effective if the frequency range (bandwidth) is sufficiently wide such that there are enough averaging pairs. The required bandwidth depends on the time difference between the interfering rays, and is given by the condition $(\Delta\Omega_{H-L} - \Delta\omega)|\Delta\tau_{m-l}| > = 2\pi$ (Worthmann & Dowling 2017), where $\Delta\Omega_{H-L}$ is the averaging bandwidth, $\Delta\omega$ is the difference-frequency and $\Delta\tau_{m-l}$ is the arrival time difference of two rays. For example, this condition is satisfied for a difference-frequency of 0.1 Hz when the signal bandwidth is $\geq$1.7 Hz for arrival-time differences of 4 s or longer.

The FDBP outputs for both averaging methods at a difference-frequency, $\Delta\omega$, are given by

$$B_{\Delta,\mathrm{BWAP}}(\underline{r}, \Delta\omega) = \left|\sum_{k=1}^{N} \overline{AP}_k(\Delta\omega) w_k(\underline{r}, \Delta\omega)\right|^2 \tag{8}$$

and

$$B_{\Delta,\mathrm{non-BWAP}}(\underline{r}, \Delta\omega) = \left\langle \left|\sum_{k=1}^{N} AP_k(\bar{\omega}, \Delta\omega) w_k(\underline{r}, \Delta\omega)\right|^2 \right\rangle_\omega . \tag{9}$$

The final backprojection results can be obtained by averaging over a range of difference-frequency pairs to increase the robustness of the results (Douglass *et al.* 2017). The FDBP backprojection images in this study are obtained from

$$B_\Delta(\underline{r}) = \left\langle B_\Delta(\underline{r}, \bar{\omega})\right\rangle_{\Delta\omega} \tag{10}$$

which varies for different stacking time windows and can be used to track earthquake rupture propagation.

3 DATA AND METHODS

In this section, we describe the data processing steps for synthetic and observed waveforms. We also outline the practical implementations of CTBP and FDBP for the synthetic cases and the 2015 M_w 7.8 Gorkha earthquake (main shock). We first benchmark our FDBP main shock results with the images obtained from CTBP by designing resolution and uncertainty analyses. The benchmark exercises use both synthetic and observed seismograms. We also

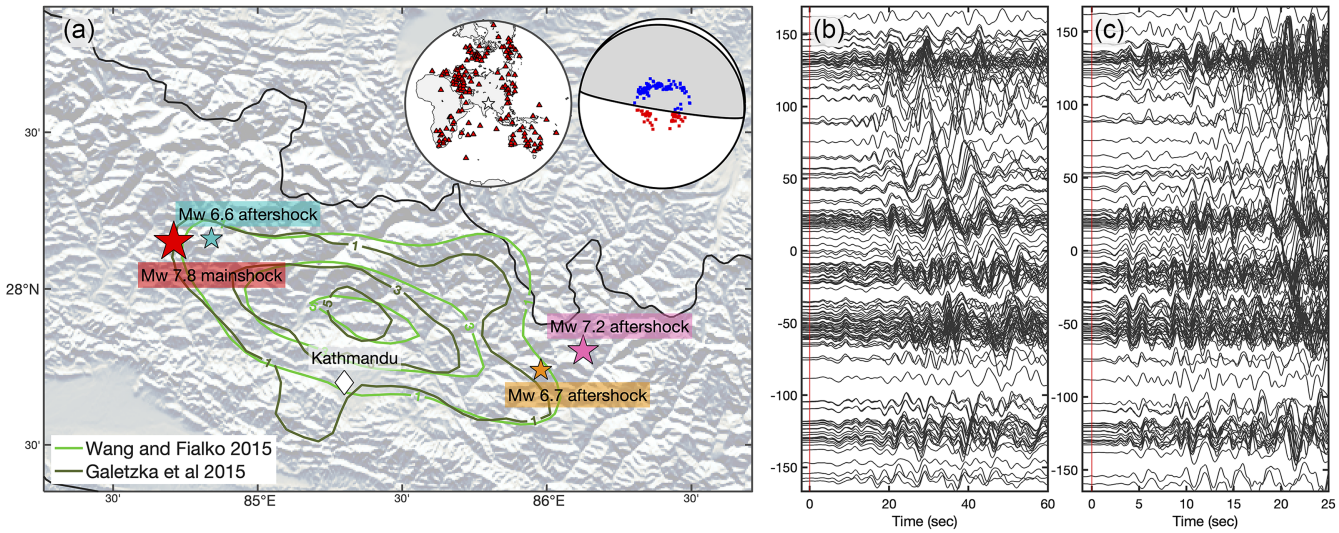

Figure 2. The 2015 *M* 7.8 Gorkha Nepal earthquake and its waveforms. (a) Map view of the source region and its three large aftershocks. Contours show finite-fault models of Wang & Fialko (2015) and Galetzka *et al.* (2015) (slip of 1–6 m with 2-m intervals). Left inset shows the stations used in this study. Right inset shows the main shock focal mechanism (Guy *et al.* 2015). The red squares in the focal mechanism indicate the compressional first motion data from the stations, while the blue squares represent the tensional data. (b) Low frequency (0.05–0.5 Hz) waveforms, first 60 s. (c) High frequency (0.3–2Hz) waveforms, first 25 s. The waveforms are self-normalized by the first 15 s and arranged by the station azimuth (vertical-axis).

bootstrap the records to statistically analyse the result sensitivity to the global array configuration.

3.1 Seismic data selection and processing

For synthetic seismograms, we use the Ricker wavelet to approximate *P*-wave pulses. The Ricker wavelet has a constant phase over 0.3–2 Hz for a peak frequency of 1 Hz. The constant phase simplifies the implementation of BWAP (Worthmann & Dowling 2017), and such an exercise helps to isolate the effects of inaccurate traveltimes in the backprojection images. A single Ricker wavelet (Ricker 1953) in the time domain is defined as

$$d_{\text{Ricker}}(t) = \left(1 - \frac{1}{2}(2\pi f_p)^2 t^2\right) \exp\left(-\frac{1}{4}(2\pi f_p)^2 t^2\right), \tag{11}$$

where f_p is the peak frequency (Hz) and t denotes time. For a multiple-source case, synthetic seismograms of each source are generated independently and then summed together at each station.

For analyses based on real earthquake seismograms, we download globally distributed, vertical-component, broad-band *P*-wave records from the Data Management Center of the Incorporated Research Institutions for Seismology (see Data Availability), including records of M_w 6.6 (2015/04/25) and M_w 6.7 (2015/04/26) aftershocks, and those of the 2015 M_w 7.8 Gorkha earthquake (Fig. 2a). The stations are within 30–90° epicentral distance from the respective epicentres. In total, we use 155 unique stations to image the 2015 Gorkha main shock and 45 stations for the aftershock test. To compare our M_w 7.8 Gorkha earthquake results to other studies, we evaluate the seismograms in two frequency bands, 0.05–0.5 Hz (low frequency, LF, Fig. 2b) and 0.3–2 Hz (high frequency, HF, Fig. 2c). The seismograms are filtered with a zero-phase 4th order Butterworth filter. Theoretically, filtering is not needed to apply backprojection in the frequency domain. Practically, we find that filtering improves both the CFBP and FDBP images. We speculate that filtering can suppress noise in the seismograms, which results in cleaner images. For each frequency band, the filtered records with signal-to-noise ratios (SNR) less than 3 are discarded. The SNR is defined as the RMS amplitude ratio from time windows 10 s before and 10 s after the theoretical *P*-wave arrival obtained from the IASP91 model (Kennett & Engdahl 1991). To balance the station distribution, we group stations into 1° azimuthal bins and only select the first record in each bin, which are sorted by alphabetical order, for the backprojection analyses. Finally, the records are visually examined, and we only keep the ones that have clear, simple *P*-wave onsets.

To reduce impacts from 3-D Earth velocity structures, we empirically correct possible traveltime errors by aligning the waveforms before the backprojection analyses. The waveforms are aligned using a multichannel cross-correlation method for the two frequency bands independently (VanDecar & Crosson 1990; Shearer 1997; Hauksson & Shearer 2005). In this method, we construct linear inverse problems using the differential times obtained from pairwise cross-correlations, weighting each pair by their cross-correlation coefficients. The optimal set of values (time correction) minimizes the ℓ_1 misfit, and are calculated using convex optimization (e.g. CVX package, Grant & Boyd 2008). The final optimal time corrections are obtained after iteratively repeating this inversion procedure using different window lengths, where subsequent iterations of alignment are based upon the previous corrections. Low-frequency records are aligned after two iterations using time windows of –8 to 8 s and 0–6 s relative to the theoretical *P*-wave arrival. High-frequency records are aligned after three iterations, using time windows of 1.5–8, 0–6 and 0.6–1.7 s. These windows are visually selected to align the waveforms using the earliest strong pulses. In addition, the HF time-shifts of stations NWAO and KOM are manually corrected.

We also generate composite seismograms as 'synthetic' data by summing real seismic records of the M_w 6.6 and 6.7 aftershocks. The two earthquakes have similar focal mechanisms to that of the main shock (United States Geological Survey solutions; Guy *et al.* 2015). The first aftershock is located close to the main shock epicentre while the second aftershock is near the eastern end of the slip distribution (Fig. 2a). The records are filtered at 0.3–2 Hz, and waveforms of the two events recorded by the same station are scaled by a set of amplitude ratios. The amplitude ratio is defined as the strength

of the first source to that of the second source (see Section 4.1 for details), and it is calculated by the ratio of peak amplitudes of the first 25 per cent of the record (i.e. the normalization factor for each trace; see Section 3.2 for details). They are then summed together from 40 s before to 60 s after their predicted *P* wave arrivals, with a 15 s delay for the second event. We adopt the same set of empirical time corrections obtained for the M_w 6.6 earthquake for later analyses. The time corrections are different for the two earthquakes at the same station, which is likely due to the near-source small-scale 3-D velocity structures. Hence, applying backprojection analyses to the composite 'synthetic' data will allow us to examine realistic effects of multiple paths, reflections, and signal-generated noise.

3.2 Backprojection analyses

We apply CTBP and FDBP methods to both the synthetic and observed seismograms to compare their results. The waveforms are processed in the same way for the two analyses. The waveforms are self-normalized by the maximum amplitude of the first few seconds of the *P* waves to remove effects from site conditions, radiation pattern, and instrument gains. The normalizing window is set as 25 per cent of the record length used in our imaging analyses, which is 6 s for the synthetic tests and 15 s for the 2015 Gorka main shock. To locate potential sources, we set source grids of 400 km by 400 km with a 5 km spacing covering an area of 26.4–30.0° and 82.8–86.9° in latitude and longitude. The grids are fixed at the hypocentral depth of 10 km. The same set of source grids are used for all the analyses, including the uncertainty analyses. Theoretical *P*-wave traveltimes of the grids are computed using the IASP91 velocity model (Kennett & Engdahl 1991).

For CTBP, we apply the *N*th root stacking approach to enhance coherent signals with small amplitudes at the cost of absolute amplitude information (McFadden *et al.* 1986). The non-linear stacking strategy has been successfully implemented in backprojection analyses, and we use $N = 4$, which has yielded well-resolved results (e.g. Xu *et al.* 2009). Evolution of the rupture process can be inferred from the snapshots of the backprojection energy bursts. Here we use a snapshot window length of 15 s with a 5 s increment step starting from –7.5 s. Ideally, a short time window would allow imaging of the rupture process at a higher temporal resolution. However, a longer time window would increase the resolution of backprojection images by reducing the impacts of incoherent noise and ensuring higher stability in the results. To select the optimal window length for the 2015 Nepal earthquake, we have experimented with lengths of 10, 15 and 20 s. We find that using a 10 s time window would adversely impact the results, especially for the low frequency band (0.05–0.5s). As the imaging results are similar for the 15 and 20 s time windows, we opt to use the 15 s window length.

For CFBP and FDBP, we use the same set of imaging parameters as for CTBP, including the start time, time step and time window length. We apply a reference point time-windowing strategy to CFBP and FDBP as detailed in Section 2 to ensure that coherent phases recorded by all stations can be used to image rupture propagation for the same time windows. The theoretical traveltime $\tau_k(\underline{r}^{\mathrm{ref}})$ from the peak location of the previous time window is used to determine the onsets of the following time windows for each station. We empirically select the $\Delta\omega$ ranges as 0.067–0.133 Hz for the Ricker test and 0.067–1.6 Hz for the aftershock tests by trial and error. For the main shock analysis, we opt to use $\Delta\omega$ of 0.07–0.4 Hz for the LF band and 0.13–0.87 Hz for the HF band, which is kept the same for the two FDBP averaging approaches. These values are empirically selected to enhance the FDBP images. We also statistically examine the backprojection results by bootstrapping the stations for the synthetic tests and main shock case study.

To interpret the FDBP results, we compare the normalized peak power time functions for both FDBP averaging approaches to the normalized moment rate function. The normalized peak power time functions for FDBP are calculated using a time window length of 15 s and an increment time step of 1 s. The moment rate function is obtained from the finite-fault model of Galetzka *et al.* (2015), and is normalized by the peak moment rate for visual comparisons.

4 RESULTS

4.1 Resolution and uncertainty

As described in Section 1, there are intrinsic ambiguities in backprojection images. To understand the accuracy and uncertainty of our results, we conduct three types of synthetic tests to assess the impacts of traveltime errors, array configuration, and signal-generated noise on FDBP images before comparing the main shock results to previous studies. In all tests, we use the epicentres of the M_w 6.6 and 6.7 aftershocks as the synthetic source locations and assume a 15 s temporal separation between the two sources. The synthetic seismograms are computed for the same set of stations as shown in Fig. 3(a). We apply CTBP, CFBP and FDBP to the Ricker wavelet synthetic seismograms and composite 'synthetic' data to resolve the two sources.

In Test 1, we generate Ricker wavelet synthetic seismograms and filter the records at 0.3–2 Hz. To simulate effects of 3-D Earth structures, we perturb the arrival times of pulses from the second source by adding random traveltime errors. The errors are drawn from zero-mean normal distributions, with a range of standard deviations (SE) increasing from 0 to 4 s. Current 1-D models can generally predict the arrival times accurately with a SE $\leq$ 2 s (Kennett & Engdahl 1991). Therefore, the broad range of our testing values includes some extreme cases, and they are used to examine the limits of the backprojection methods. For each assumed normal distribution, 1000 realizations are sampled and their backprojection results are evaluated. To make a quantitative evaluation of the results, we define the distances between the peak energy loci and the input source locations as the location error, which is then averaged for the 1000 realizations. We refer to this average as the mean location error and the standard deviation of the 1000 location errors as the location uncertainty for this test.

Test 1 (Fig. 3b) shows that FDBP is able to locate the second source with a smaller mean location error compared to CTBP. We also find that CFBP has the largest error among all methods. For example, for SE = 2 s, the FDBP results have a mean location error of ~0.2° while the CTBP and CFBP results have errors of around 0.6° and 1.4°, respectively. When the traveltime errors are drawn from a distribution with SE = 4 s, the mean location errors of FDBP and CTBP are similar. It is probably because the accuracy of the results are limited by the values of $\Delta\omega$. Hence, the results show that for the $\Delta\omega$ range used in the analysis (0.067–0.133 Hz), FDBP would not have an advantage over conventional backprojection for traveltime errors larger than or equal to extreme scenarios of SE = 4 s. The location uncertainty of FDBP is greater than that of CTBP when SE $\geq$ 2.7 s (Figs 3b and c), showing that the FDBP methods can have lower resolutions even though they have equal or greater accuracy in resolving the seismic sources.

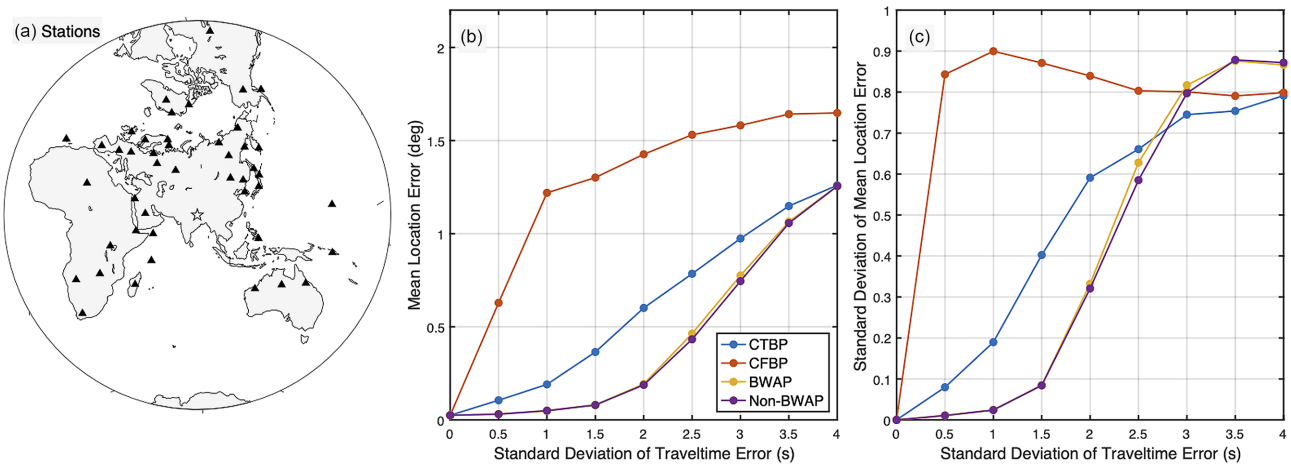

Figure 3. Comparison of backprojection results of conventional time-domain backprojection, conventional frequency-domain backprojection, FDBP (BWAP) and FDBP (non-BWAP) using synthetic Ricker wavelet seismograms (Test 1). Random traveltime errors are added to the synthetic waveform arrivals, which are drawn from zero-mean normal distributions with varying standard deviations. For each assumed error distribution, the imaging exercises are performed for each method with 1000 realizations of the random traveltime errors. A difference-frequency range of 0.067–0.13Hz is used for the FDBP methods. (a) Station map of the synthetic test. Black triangles are the stations. A white star indicates the centroid of the two sources. (b) Mean location error versus standard deviation of the traveltime error. (c) Standard deviation of mean location error (i.e. location uncertainty of the traveltime error).

We examine the sensitivity of the methods to array configuration in Test 2. We bootstrap the stations for a set of Ricker wavelet seismograms that are computed including the traveltime errors from a zero-mean normal distribution with SE = 2 s. The SE value is selected for the test because it would lead to a mean location error of ∼0.6° for CTBP results as shown in Test 1. This location error is comparable to empirically observed values using conventional approaches (e.g. Fan & Shearer 2017). Specifically, we randomly resample the stations following a uniform distribution to obtain an array with the same number of stations, and repeat the CTBP, CFBP and FDBP backprojection analyses for 1000 times, respectively. We quantify the image uncertainties as the standard errors of the deviation from the mean peak energy location from the 1000 realizations. It is worth noting that these peak energy loci are not necessarily the same as the input locations.

Figs 4(a)–(d) show the bootstrapping results of the Ricker synthetic test (Test 2). The crosses in the figure demonstrate the locations of the backprojection peak energy loci when all the stations are used. When the traveltime error is added to the arrival times of the second pulse, the conventional backprojection methods tend to mislocate the second source, whereas the FDBP methods can accurately locate the second source. We find that CTBP and FDBP produce similar standard errors ranging from 0.62° to 0.86°. We also observe that using lower values of $\Delta\omega$ leads to more accurate results but more smeared images as explained in Section 2.2. Moreover, using a larger range of $\Delta\omega$ leads to lower standard errors. These results validate our numerical implementation of FDBP.

The simple waveforms of the Ricker wavelet do not reassemble the real observations, which often contain coda waves and noises that arise from random sources or structural scatterers. Such signal-generated noises are coherent and may cause artefacts that are difficult to distinguish from true rupture features. Hence, we design Test 3 using real waveforms and apply the CTBP, CFBP and FDBP imaging methods following the procedure described in Section 3.2.

Here we use the composite 'synthetic' seismic records from the M_w 6.6 and 6.7 aftershocks for Test 3. The composite records include pre-*P*-wave noises and *P*-wave coda waves of the two earthquakes. The coda waves from the first source overlap with the arrival of the second source, and the resolvability of the second source strongly depends on the relative *P*-wave amplitudes. If we set the amplitude ratio of the first source to the second source to be 0.5, as shown in Figs 4(e)–(h), the FDBP method can locate the second source using either of the averaging approaches (BWAP or non-BWAP), while CTBP and CFBP fail to do so. When the amplitude ratio is set as 0 (i.e. mute the first event), CTBP can resolve the second source accurately due to the lack of noise from the first event (see Fig. S1 for more details). CFBP cannot locate the second source accurately even when the first source is muted, but it can resolve the second source when there is no traveltime error, suggesting that CFBP is more sensitive to traveltime error than the other methods. The results show that FDBP is less sensitive to the noise and traveltime error than conventional approaches. However, CTBP and FDBP obtain similar standard errors from bootstrapping while CFBP has slightly larger standard error. Hence, we find that that standard error is useful in describing the range of solutions for a given data set, but the metric does not address the solution accuracy.

Additionally, we perform depth-phase tests to determine if they would introduce significant uncertainties in the source locations (see Fig. S2 for details). We compute synthetic waveforms to include the pP and sP depth phases for two point sources following the procedure outlined in (Fan & Shearer 2015). We find that depth-phases have minor impacts on the FDBP and conventional backprojection images. We also experimented using a single-time-reference strategy for both conventional frequency-domain backprojection and FDBP. We find that the backprojection results would only change marginally compared to our proposed multi-time window strategy. As shown in Meng *et al.* (2012a), multitime window approach may be advantageous for imaging large earthquakes, and we opt to use the multi-time window strategy to image the 2015 Nepal earthquake. FDBP assumes that relative phases are consistent throughout the bandwidth, but 3-D Earth structures are heterogeneous at various length scales. Therefore, we examine this impact by swapping the time corrections from two different frequency bands and imaging the earthquake using the waveforms in the other frequency band (see Fig. S3 for details). We find that swapping time corrections

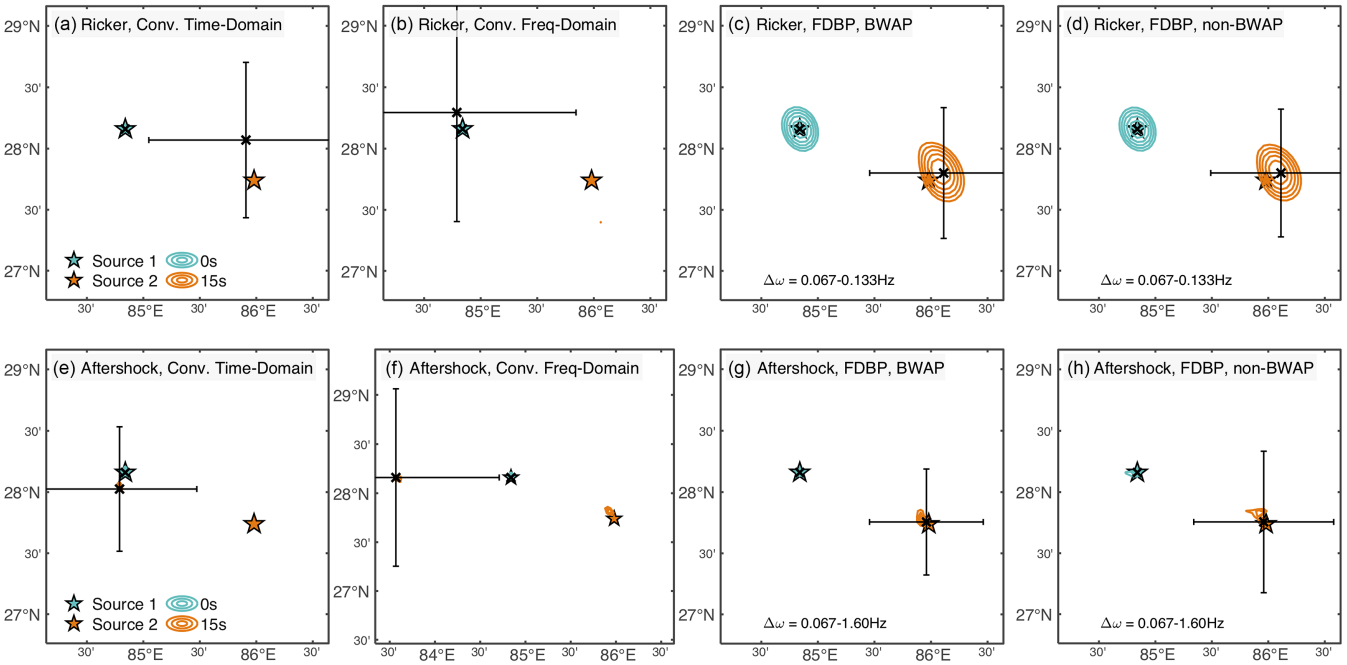

Figure 4. Results of Test 2 (top row, a–d) and Test 3 (bottom row, e–h) for four backprojection methods (columns). The stars indicate the locations of the two input sources, contours show the normalized backprojection output from 80:4:100, and crosses mark the peak-power locations of the backprojection images (calculated using all stations). Error bars show the standard errors from bootstrapping stations for resolving the second source loci. The FDBP results locate the second source more accurately for both tests.

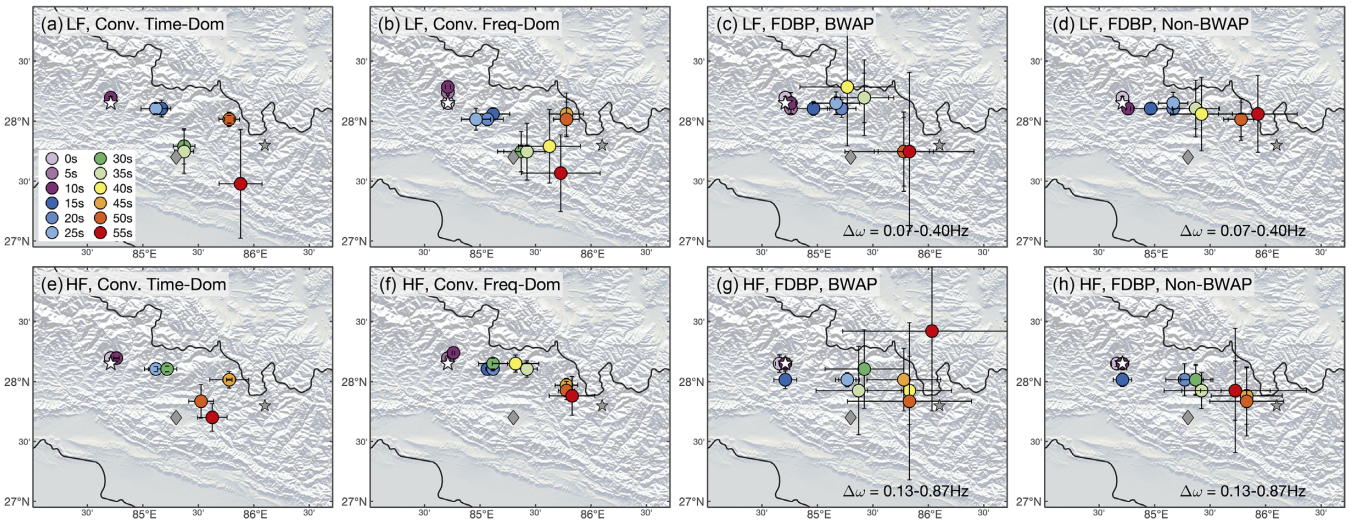

Figure 5. Backprojection results of the 2015 Gorkha, Nepal main shock. The four columns show results of CTBP (a, e), CFBP (b, f), BWAP (c, g) and non-BWAP (d, h). The top row (a–d) shows the low frequency (LF; 0.05–0.5 Hz) snapshot results. The bottom row (e–h) shows the high frequency (HF; 0.3–2 Hz) snapshot results. The centroid time of each time window is indicated in the legend. The standard errors of the peak loci are shown as the error bars. The white star, grey diamond and grey star indicate the main shock epicentre, Kathmandu, and the *M*7.3 aftershock epicentre, respectively.

have generally minor effects on the results, and the main rupture characteristics are well resolved.

We find that both BWAP and non-BWAP work well for a large range of $\Delta\omega$. This shows that for transient seismic sources, FDBP is a feasible method as long as we stack over a wide range of frequencies for the given time windows. In summary, the synthetic tests show that FDBP may have advantages over CTBP when the records are noisy and may be better suited to image later rupture stages of large earthquakes when seismic radiations are likely obscured by coda waves.

4.2 Backprojection images of the 2015 M_w 7.8 Gorkha earthquake

We present the imaging results of the 2015 M_w 7.8 Gorkha earthquake using the CTBP, CFBP and FDBP (BWAP and non-BWAP) methods in two frequency bands (0.05–0.5 Hz, LF and 0.3–2 Hz, HF, Fig. 5). For comparison, we select the same set of $\Delta\omega$ values for both BWAP and non-BWAP, although the two methods may not necessarily have the same optimal $\Delta\omega$ values. The CTBP (Figs 5a and e) and CFBP (Figs 5b and f) approaches yield similar results as

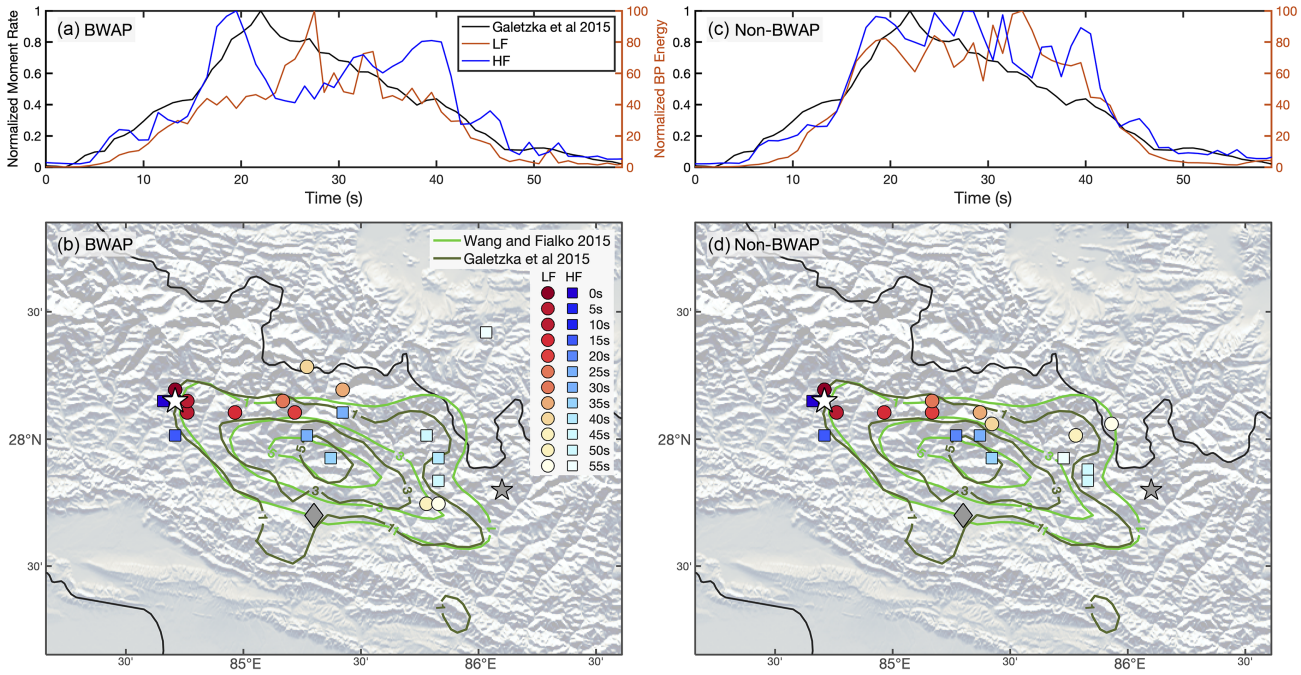

Figure 6. Comparison of the FDBP results with finite-fault slip models. (a) Normalized FDBP BWAP peak power time functions and moment-rate function from Galetzka *et al.* (2015). (b) FDBP BWAP results and finite-fault slip models (Wang & Fialko 2015; Galetzka *et al.* 2015). The LF and HF FDBP results are shown as red and blue circles, respectively. The centroid time of each time window is indicated in the legend. The finite-fault slip models (Wang & Fialko 2015; Galetzka *et al.* 2015) are shown with contours of 1:2:6 m. The white star, grey diamond and grey star are the main shock epicentre, Kathmandu, and the *M*7.3 aftershock epicentre, respectively. Panels (c) and (d) are FDBP non-BWAP results, sharing similar legends as of (a) and (b).

reported by previous studies (e.g. Fan & Shearer 2015; Avouac *et al.* 2015). Here we focus on the FDBP results and highlight the new features. We find that both the BWAP (Figs 5c and g) and non-BWAP results (Figs 5d and h) can capture the general rupture process of the 2015 M_w 7.8 Gorkha earthquake, but with some variation in the details of the snapshots.

The LF FDBP BWAP snapshot results (Fig. 5c) show three distinct rupture stages: a slow initial stage for the first 10 s, a linear propagation to the east from 15 to 40 s, and a final termination stage for the last 15 s. The initial stage features a slow rupture development with an apparent rupture speed that is almost stationary. This is manifested in the first 10 s waveforms that show little moveout (Fig. 2c). The rupture then propagated eastwards and seemed to slow down in the second stage. Finally, the backprojection images suggest a somewhat chaotic termination stage, showing an apparent jump in rupture location towards the updip/south direction (i.e. shallower depth). The LF BWAP snapshot results share similar features to those from the CTBP and LF CFBP methods, but the peak energy loci during 30–35 s seem to be located at deeper depths (Fig. 5c). The HF BWAP snapshots (Fig. 5g) are similar to the LF BWAP results, suggesting a slow initial rupture and a generally linear eastward propagation. Additionally, the peak power loci seem to cluster around the hypocentre, the peak slip location of the earthquake, and the eastern end of the slip distribution, where the rupture likely transitioned between stages.

The FDBP non-BWAP results are similar for both the HF and LF bands. The snapshots suggest that the rupture was almost stationary for the first 10 s. From 10 to 55 s, the rupture propagated continuously in a linear fashion eastward and terminated smoothly at the slip distribution edge (Figs 5d and h). In comparison to other images, the non-BWAP snapshots are located further down-dip and the results do not suggest an abrupt up-dip rupture transition in the last stage.

The location uncertainties (i.e. standard error of the peak locations) from the bootstrapping analysis are visualized as error bars in Fig. 5. As shown in Test 3 (Fig. 4), the error bars likely represent the data coherence, and the standard errors do not necessarily correlate with the accuracy of the results. For all methods, the standard error is less than 0.21° for the peak loci of the first 25 s of the snapshots. The standard error increases as the rupture progresses, which may relate to the interference from coda waves or traveltime errors from near-source heterogeneities. We observe that the CTBP and CFBP results have smaller location standard errors compared to the FDBP results, and the non-BWAP results have smaller standard errors compared to those of BWAP. The LF CTBP and CFBP results have larger standard errors compared to their HF results, whereas the standard errors of the two frequency bands are comparable for the FDBP results.

The FDBP non-BWAP normalized peak power-time functions (the 'peak' refers to space) and the normalized moment rate function from Galetzka *et al.* (2015) share similar patterns, while the FDBP BWAP normalized power-time functions is slightly different, showing clear peaks at ∼27 s for LF and ∼20 s for HF results (Figs 6a and c). Back-projection normalized peak power time functions often have different patterns compared to the finite-fault moment rate functions, and our results show that FDBP might help to connect high-frequency seismic radiation to lower frequency seismic slip. The HF FDBP normalized peak power time functions for both methods also suggest a second peak around 40 s compared to that of Galetzka *et al.* (2015). In general, the BWAP and non-BWAP FDBP peak loci are all located within the 1 m slip contours of finite-fault models from the Wang & Fialko (2015) and

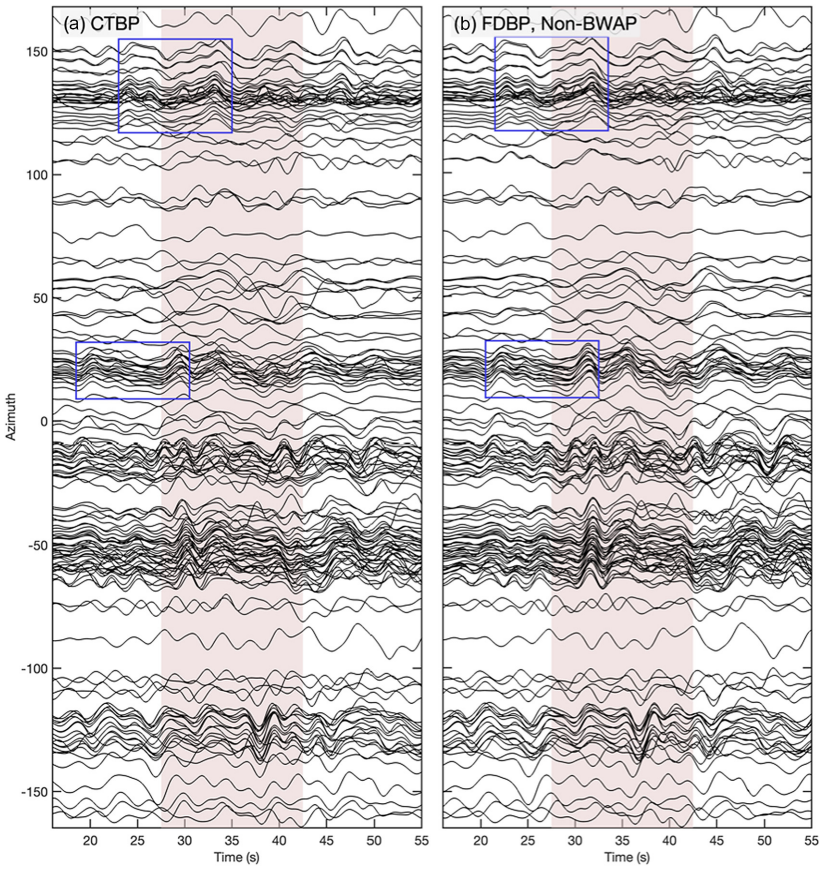

Figure 7. LF waveforms aligned using peak loci of the time window 27.5–42.5 s. (a) The alignment is based on the CTBP peak power location. (b) The alignment is based on the FDBP non-BWAP peak power location. The time window is shown as the red patch in the background and the waveforms are self-normalized by their first 35 s. Blue boxes highlight similar sets of pulses for visual comparisons.

Galetzka *et al.* (2015) (Figs 6b and d), and the LF loci tend to trace the downdip edge of the slip.

5 DISCUSSION

The main shock rupture features are imaged consistently using the CTBP, CFBP and FDBP methods in the high frequency band (0.3–2 Hz), including the three main rupture stages as described in Section 4.2. These features are also reported in previous backprojection and finite-fault inversion studies (e.g. Fan & Shearer 2015; Grandin *et al.* 2015; Yagi & Okuwaki 2015; Avouac *et al.* 2015; Galetzka *et al.* 2015; Wang & Mori 2016), confirming the robustness of our results. The general good agreement between the CTBP, CFBP and FDBP images supports the feasibility of the FDBP method. Additionally, the location uncertainties in the CTBP and LF non-BWAP results are low, with most loci standard errors less than 0.2°. These results suggest that the FDBP images are robust.

Details of the CTBP, CFBP and FDBP snapshots of the 2015 Gorkha earthquake differ from each other for a few time windows. For example, the peak LF CTBP and LF CFBP radiation around 35 s is located updip near Kathmandu, but this is not observed in the FDBP results. To investigate this difference, we realign the LF waveforms at time window 8 (centred at 35 s) based on the peak loci of the CTBP and FDBP non-BWAP results. As shown in Fig. 7, the waveforms appear to be more coherently aligned using the FDBP loci compared to CTBP. The observed differences in snapshots can be caused by the different ways that each method measures coherence. CTBP and CFBP evaluate the coherence of the amplitude and phase of the waves, respectively. FDBP measures the coherence of the autoproduct (the phase-difference) at each station, and may be more robust to noise and traveltime errors. The peak power location of the final time window is also different for each method, but re-alignment of the waveforms based on the locations does not show a clear difference in waveform coherence. This is likely because the signal is weaker at the end of the rupture, and tends to be obscured by coda waves. The different ways of measuring coherence could also explain the clustering pattern observed in the CTBP snapshots. CTBP loci could be more influenced by pulses with large amplitudes in the time domain, while CFBP and FDBP measure the phases and may be more sensitive to the shape of the pulses. CTBP also considers a different time-windowing scenario of every gridpoints, while CFBP and FDBP use the reference-window strategy and use the same time window for all gridpoints. This means that additional pulses are more likely to be included in the stacking time-windows for CTBP, resulting in the spatially clustered peak power loci of the snapshots.

We also find that the two averaging approaches, BWAP and non-BWAP, appear to lead to different results with different implementations. Both averaging approaches perform equally well for our synthetic tests (Fig. 3). However, for the 2015 Gorkha main shock, the non-BWAP results have lower location uncertainties and suggest a continuous, linear rupture propagation, which differ from those of the BWAP results (Fig. 4). In contrast, previous acoustic studies find that BWAP is superior at locating sources than non-BWAP (Douglass *et al.* 2017). The variations in performances may result

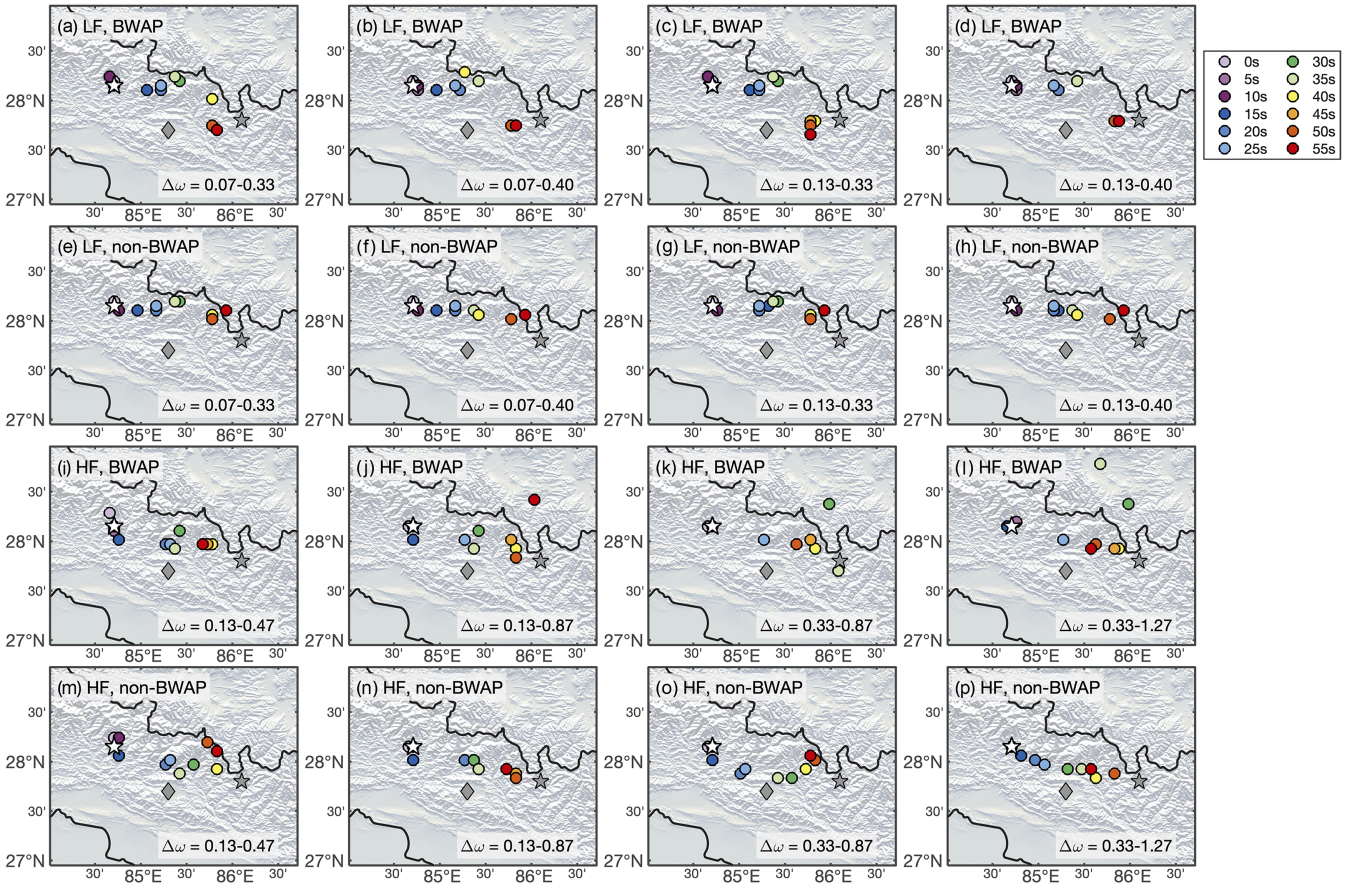

Figure 8. FDBP BWAP and non-BWAP results of different $\Delta\omega$ ranges (each column displays a different range of $\Delta\omega$, which is shown on the bottom right of each panel). The top two rows show the backprojection results of using low frequency waveforms, while the bottom two rows show the results of using high frequency waveforms. The coloured dots represent the backprojection peak-power loci of the time windows, of which centroid times are indicated in the legend. The white star, grey diamond and grey star show the *M*7.8 main shock epicentre, Kathmandu and the *M*7.2 aftershock epicentre, respectively.

from the complexities in the source characteristics. For example, the acoustic experiments have an idealized laboratory experiment setup, and the Test 3 experiment also uses simple point sources. In the acoustic experiments, the sources are static and emit Gaussian-windowed chirp pressure waves with frequencies over a hundred of kilohertz (Lipa *et al.* 2018). The media (water) is homogeneous, and the boundary conditions are given. On the other hand, large earthquakes can rupture over hundreds to thousands of kilometres and radiate seismic waves in complex ways (Ishii *et al.* 2005; Lay *et al.* 2005). Given the Gorkha main shock ruptured over 160 km, its seismic radiation is likely caused by complex rupture processes (Galetzka *et al.* 2015; Whipple *et al.* 2016; Elliott *et al.* 2016). Hence, the phase of seismic radiation from the Gorkha main shock may not be constant over the bandwidth, resulting in the lack of coherence of the autoproduct for each frequency-pair and causing a difference in the performance of BWAP. The two stacking strategies are based on different assumptions that causes them to have complementary advantages: BWAP is more suitable to resolve smooth ruptures of earthquakes in regions with highly heterogeneous velocity structures, while non-BWAP is likely advantageous in imaging complex earthquakes rupture processes. It is useful to apply both stacking approaches to the same earthquake and compare the results to infer the rupture processes. For the case study of the Gorkha main shock, it is remarkable that FDBP can be successfully used to image earthquake rupture processes despite the great differences among different sources.

As the range of $\Delta\omega$ used in FDBP directly impacts the results, we evaluate the FDBP images for a few $\Delta\omega$ ranges (Fig. 8). We find that the variations are small for the low-frequency band if we choose a sufficiently wide range of $\Delta\omega$ (e.g. 0.067–0.33 Hz). Furthermore, we find that the FDBP non-BWAP results (Figs 8e–h, m–p) seem to be less impacted by the $\Delta\omega$ ranges compared to the FDBP BWAP results (Figs 8a–d, i–l). The optimal range likely depends on the earthquake source attributes and FDBP averaging strategy. For example, if there is a larger amount of near-source heterogeneity resulting in greater traveltime errors, smaller $\Delta\omega$ values should be preferred to produce more accurate results. Hence, one strategy would be applying FDBP to small earthquakes in the region to estimate an optimal $\Delta\omega$ range before imaging the earthquakes of interest. Earthquake magnitude and its stress drop would influence the source spectra, which would also impact the optimal bandwidth for implementing FDBP. Finally, multipathing would impact the optimal $\Delta\omega$ values for BWAP as the time-delays between the direct and reflected phases would inversely correlate with the optimal $\Delta\omega$ values (Section 2.2). The topic warrants future investigations using realistic synthetic 3-D wavefields.

As determining the $\Delta\omega$ range can be subjective, the FDBP method relies on expert opinions in choosing these values. However, FDBP has the advantage of being less sensitive to the unknown near-source velocity structures compared to conventional approaches. Even though both conventional backprojection and FDBP use a known velocity model to predict the phase arrivals, conventional

backprojection requires the velocity model to be valid in the signal bandwidth, while FDBP requires the model to be valid in the (typically lower) $\Delta\omega$ bandwidth. Given that large scale structures are often better resolved, the wave scattering due to complex structures at high frequency would cause the conventional methods to be less accurate. Thus, FDBP has potential in using high frequency seismic records for imaging the rupture processes of moderate magnitude earthquakes, which are best recorded at regional arrays with highly heterogeneous velocity structures. Moreover, FDBP may mitigate the impact of varying focal mechanisms during earthquake ruptures, as the phase-differences of frequency pairs are not affected by the variation of radiation pattern, such as the *P*-wave polarity.

It is critical to understand the robustness of the backprojection images before interpreting the results. Most main shock rupture features (for the first 50 s) obtained from the FDBP non-BWAP method are consistent using both the HF and LF bands, and the peak power loci have standard errors that are less than 0.33°. This is comparable to empirical uncertainties estimated using small ($\sim M6$) earthquakes for conventional backprojection results, confirming the robustness of the images (Fan & Shearer 2017). Different from the synthetic tests results, the Gorkha main shock FDBP results have higher standard errors compared to those of CTBP and CFBP. The bootstrap tests can provide a formal way to examine the model sensitivity to a given array configuration with the 3-D Earth effects. However, standard errors from the bootstrap tests do not distinguish model accuracy and uncertainty. As shown in Test 3, a low standard error primarily suggests that the results are insensitive to the array geometry, but it does not imply the results are more accurate (Fig. 4).

With the imaging exercises, we find that both the conventional backprojection and FDBP approaches can be effective in imaging earthquake rupture processes, and they both have unique merits in resolving different rupture features. Conventional backprojection is operationally simple, and it can be easily implemented for simple earthquakes occurring in regions where the velocity structure is well-known. Our investigation of the Gorkha earthquake shows that FDBP can provide a first-order estimate of the rupture process. The synthetic tests suggest that FDBP has the potential to improve the robustness of backprojection results because it is less sensitive to scattering and traveltime errors. These advantages would be particularly useful for resolving earthquake rupture processes in structurally complex regions. By imaging earthquakes with different methods and collectively analysing the models, we could potentially improve our understanding of earthquake rupture processes.

6 CONCLUSION

We have developed a novel FDBP approach in the frequency domain to image earthquake rupture processes. We further explore two different stacking strategies of FDBP, BWAP and non-BWAP, which stack the spectra incoherently and coherently. The FDBP method has potential in improving seismic radiation location accuracy. From systematic uncertainty quantification exercises, we find that FDBP can reduce the impacts of inaccurate traveltime errors as well as coda wave interference. We successfully apply FDBP to image the 2015 Gorkha M_w 7.8 earthquake in two frequency bands, and its main rupture features are robustly resolved. The FDBP results resemble those of conventional backprojection methods, and most of the obtained peak radiation loci have less than 0.33° standard deviations. The two stacking approaches reveal different details of the Gorkha earthquake rupture process, and the non-BWAP images are more stable and have lower standard error in the peak power loci. We also find that the choice of $\Delta\omega$ ranges impacts the FDBP results. Our results suggest that the FDBP method is promising in resolving complex earthquake rupture processes in tectonically complex regions, and the method can potentially be applied to image moderate magnitude earthquake rupture using regional arrays and high frequency seismic records.

ACKNOWLEDGMENTS

We thank the editor Eiichi Fukuyama and four anonymous reviewers for their thoughtful and constructive feedback, which has greatly improved the study. JCN and YH acknowledge funding from the NSF grant EAR-1943742. WF acknowledges funding from NSF grant EAR-2022441. We are grateful to Dr Diego Melgar and Dr Kang Wang for sharing their finite-fault slip models and Dr Jeroen Ritsema for his helpful comments and suggestions.

DATA AVAILABILITY

The seismic data were provided by Data Management Center (DMC) of the Incorporated Research Institutions for Seismology (IRIS). The facilities of IRIS Data Services, and specifically the IRIS Data Management Center, were used for access to waveforms, related metadata and/or derived products used in this study. IRIS Data Services are funded through the Seismological Facilities for the Advancement of Geoscience and EarthScope (SAGE) Proposal of the National Science Foundation (NSF) under Cooperative Agreement EAR-1261681.

REFERENCES

Abadi, S.H., Song, H.C. & Dowling, D.R., 2012. Broadband sparse-array blind deconvolution using frequency-difference beamforming, *J. acoust. Soc. Am.,* **132**(5), 3018–3029.

Avouac, J.-P., Meng, L., Wei, S., Wang, T. & Ampuero, J.-P., 2015. Lower edge of locked main Himalayan thrust unzipped by the 2015 Gorkha earthquake, *Nat. Geosci.,* **8**(9), 708–711.

Douglass, A.S. & Dowling, D.R., 2019. Frequency-difference beamforming in the presence of strong random scattering, *J. acoust. Soc. Am.,* **146**(1), 122–134.

Douglass, A.S., Song, H. & Dowling, D.R., 2017. Performance comparisons of frequency-difference and conventional beamforming, *J. acoust. Soc. Am.,* **142**(3), 1663–1673.

Dowling, D.R., 2018. Revealing hidden information with quadratic products of acoustic field amplitudes, *Phys. Rev. Fluids,* **3**(11), doi:10.1103/PhysRevFluids.3.110506.

Elliott, J., Jolivet, R., González, P.J., Avouac, J.-P., Hollingsworth, J., Searle, M. & Stevens, V., 2016. Himalayan megathrust geometry and relation to topography revealed by the Gorkha earthquake, *Nat. Geosci.,* **9**(2), 174–180.

Fan, W. & Shearer, P.M., 2015. Detailed rupture imaging of the 25 April 2015 Nepal earthquake using teleseismic P waves, *Geophys. Res. Lett.,* **42**(14), 5744–5752.

Fan, W. & Shearer, P.M., 2017. Investigation of backprojection uncertainties with M6 earthquakes, *J. geophys. Res.,* **122**(10), 7966–7986.

Fan, W. & Shearer, P.M., 2018. Coherent seismic arrivals in the P wave coda of the 2012 Mw 7.2 Sumatra earthquake: water reverberations or an early aftershock?, *J. geophys. Res.,* **123**(4), 3147–3159.

Fan, W., Wei, S.S., Tian, D., McGuire, J.J. & Wiens, D.A., 2019. Complex and diverse rupture processes of the 2018 Mw 8.2 and Mw 7.9 Tonga-Fiji deep earthquakes, *Geophys. Res. Lett.,* **46**(5), 2434–2448.

Galetzka, J. *et al.*, 2015. Slip pulse and resonance of the Kathmandu basin during the 2015 Gorkha earthquake, Nepal, *Science,* **349**(6252), 1091–1095.

Goldstein, P. & Archuleta, R.J., 1987. Array analysis of seismic signals, *Geophys. Res. Lett.,* **14**(1), 13–16.

Grandin, R., Vallée, M., Satriano, C., Lacassin, R., Klinger, Y., Simoes, M. & Bollinger, L., 2015. Rupture process of the Mw = 7.9 2015 Gorkha earthquake (Nepal): insights into Himalayan megathrust segmentation, *Geophys. Res. Lett.,* **42**(20), 8373–8382.

Grant, M. & Boyd, S., 2008. Graph implementations for nonsmooth convex programs, in *Recent Advances in Learning and Control, Lecture Notes in Control and Information Sciences,* pp. 95–110, eds Blondel, V., Boyd, S. & Kimura, H., Springer-Verlag Limited, http://stanford.edu/ boyd/graph_dcp.html.

Guy, M.R. *et al.*, 2015. *National Earthquake Information Center Systems Overview and Integration,* US Department of the Interior, US Geological Survey Reston, VA.

Hauksson, E. & Shearer, P., 2005. Southern California hypocenter relocation with waveform cross-correlation, part 1: results using the double-difference method, *Bull. seism. Soc. Am.,* **95**(3), 896–903.

Hayes, G.P., Earle, P.S., Benz, H.M., Wald, D.J. & Briggs, R.W., 2011. 88 hours: the US Geological Survey National Earthquake Information Center response to the 11 March 2011 Mw 9.0 Tohoku earthquake, *Seismological Research Letters,* **82**(4), 481–493.

Ishii, M., Shearer, P.M., Houston, H. & Vidale, J.E., 2005. Extent, duration and speed of the 2004 Sumatra–Andaman earthquake imaged by the hi-net array, *Nature,* **435**(7044), 933–936.

Kennett, B. & Engdahl, E., 1991. Traveltimes for global earthquake location and phase identification, *Geophys. J. Int.,* **105**(2), 429–465.

Kiser, E. & Ishii, M., 2012. Combining seismic arrays to image the high-frequency characteristics of large earthquakes, *Geophys. J. Int.,* **188**(3), 1117–1128.

Kiser, E. & Ishii, M., 2017. Back-projection imaging of earthquakes, *Ann. Rev. Earth planet. Sci.,* **45,** 271–299.

Krüger, F. & Ohrnberger, M., 2005. Tracking the rupture of the Mw = 9.3 Sumatra earthquake over 1,150 km at teleseismic distance, *Nature,* **435**(7044), 937–939.

Lay, T. *et al.*, 2005. The great Sumatra-Andaman earthquake of 26 December 2004, *science,* **308**(5725), 1127–1133.

Lipa, J.E., Worthmann, B.M. & Dowling, D.R., 2018. Measurement of autoproduct fields in a Lloyd's mirror environment, *J. acoust. Soc. Am.,* **143**(4), 2419–2427.

Liu, Z., Song, C., Meng, L., Ge, Z., Huang, Q. & Wu, Q., 2017. Utilizing a 3D global P-wave tomography model to improve backprojection imaging: a case study of the 2015 Nepal earthquake, *Bull. seism. Soc. Am.,* **107**(5), 2459–2466.

Manchee, E.B. & Weichert, D.H., 1968. Epicentral uncertainties and detection probabilities from the yellowknife seismic array data, *Bull. seism. Soc. Am.,* **58**(5), 1359–1377.

McFadden, P., Drummond, B. & Kravis, S., 1986. The *n*th-root stack: theory, applications, and examples, *Geophysics,* **51**(10), 1879–1892.

Meng, L., Ampuero, J.-P., Luo, Y., Wu, W. & Ni, S., 2012a. Mitigating artifacts in back-projection source imaging with implications for frequency-dependent properties of the Tohoku-Oki earthquake, *Earth, planets Space,* **64**(12), 1101–1109.

Meng, L., Ampuero, J.-P., Stock, J., Duputel, Z., Luo, Y. & Tsai, V., 2012b. Earthquake in a maze: compressional rupture branching during the 2012 Mw 8.6 Sumatra earthquake, *Science,* **337**(6095), 724–726.

Meng, L., Zhang, A. & Yagi, Y., 2016. Improving back projection imaging with a novel physics-based aftershock calibration approach: a case study of the 2015 Gorkha earthquake, *Geophys. Res. Lett.,* **43**(2), 628–636.

Okuwaki, R. & Yagi, Y., 2018. Role of geometric barriers in irregular-rupture evolution during the 2008 Wenchuan earthquake, *Geophys. J. Int.,* **212**(3), 1657–1664.

Okuwaki, R., Yagi, Y. & Hirano, S., 2014. Relationship between high-frequency radiation and asperity ruptures, revealed by hybrid back-projection with a non-planar fault model, *Sci. Rep.,* **4**(1), 1–6.

Qin, W. & Yao, H., 2017. Characteristics of subevents and three-stage rupture processes of the 2015 Mw 7.8 Gorkha Nepal earthquake from multiple-array back projection, *J. Asian Earth Sci.,* **133,** 72–79.

Ricker, N., 1953. Wavelet contraction, wavelet expansion, and the control of seismic resolution, *Geophysics,* **18**(4), 769–792.

Rost, S. & Thomas, C., 2002. Array seismology: methods and applications, *Rev. Geophys.,* **40**(3), 2-1–2-27.

Shearer, P.M., 1997. Improving local earthquake locations using the l1 norm and waveform cross correlation: application to the Whittier narrows, California, aftershock sequence, *J. geophys. Res.,* **102**(B4), 8269–8283.

Tan, F., Ge, Z., Kao, H. & Nissen, E., 2019. Validation of the 3-D phase-weighted relative back projection technique and its application to the 2016 Mw 7.8 Kaikōura earthquake, *Geophys. J. Int.,* **217**(1), 375–388.

VanDecar, J. & Crosson, R., 1990. Determination of teleseismic relative phase arrival times using multi-channel cross-correlation and least squares, *Bull. seism. Soc. Am.,* **80**(1), 150–169.

Walker, K.T. & Shearer, P.M., 2009. Illuminating the near-sonic rupture velocities of the Intracontinental Kokoxili Mw 7.8 and Denali Fault Mw 7.9 strike-slip earthquakes with global P wave back projection imaging, *J. geophys. Res.,* **114**(B2), doi:10.1029/2008JB005738.

Wang, D. & Mori, J., 2011. Rupture process of the 2011 off the Pacific coast of Tohoku earthquake (Mw 9.0) as imaged with back-projection of teleseismic P-waves, *Earth, Planets Space,* **63**(7), 603–607.

Wang, D. & Mori, J., 2016. Short-period energy of the 25 April 2015 Mw 7.8 Nepal earthquake determined from backprojection using four arrays in Europe, China, Japan, and Australia, *Bull. seism. Soc. Am.,* **106**(1), 259–266.

Wang, D., Takeuchi, N., Kawakatsu, H. & Mori, J., 2016. Estimating high frequency energy radiation of large earthquakes by image deconvolution back-projection, *Earth planet. Sci. Lett.,* **449,** 155–163.

Wang, K. & Fialko, Y., 2015. Slip model of the 2015 Mw 7.8 Gorkha (Nepal) earthquake from inversions of ALOS-2 and GPS data, *Geophys. Res. Lett.,* **42**(18), 7452–7458.

Whipple, K.X., Shirzaei, M., Hodges, K.V. & Ramon Arrowsmith, J., 2016. Active shortening within the Himalayan orogenic wedge implied by the 2015 Gorkha earthquake, *Nat. Geosci.,* **9**(9), 711–716.

Worthmann, B.M. & Dowling, D.R., 2017. The frequency-difference and frequency-sum acoustic-field autoproducts, *J. acoust. Soc. Am.,* **141**(6), 4579–4590.

Worthmann, B.M., Song, H. & Dowling, D.R., 2017. Adaptive frequency-difference matched field processing for high frequency source localization in a noisy shallow ocean, *J. acoust. Soc. Am.,* **141**(1), 543–556.

Xu, Y., Koper, K.D., Sufri, O., Zhu, L. & Hutko, A.R., 2009. Rupture imaging of the Mw 7.9 12 May 2008 Wenchuan earthquake from back projection of teleseismic P waves, *Geochem. Geophys. Geosyst.,* **10**(4), doi:10.1029/2008GC002335.

Yagi, Y. & Okuwaki, R., 2015. Integrated seismic source model of the 2015 Gorkha, Nepal, earthquake, *Geophys. Res. Lett.,* **42**(15), 6229–6235.

Yin, J., Denolle, M.A. & Yao, H., 2018. Spatial and temporal evolution of earthquake dynamics: case study of the Mw 8.3 Illapel earthquake, Chile, *J. geophys. Res.,* **123**(1), 344–367.

Yue, H., Castellanos, J.C., Yu, C., Meng, L. & Zhan, Z., 2017. Localized water reverberation phases and its impact on backprojection images, *Geophys. Res. Lett.,* **44**(19), 9573–9580.

Zeng, H., Wei, S. & Wu, W., 2020. Sources of uncertainties and artefacts in back-projection results, *Geophys. J. Int.,* **220**(2), 876–891.

Zhang, H., Van Der Lee, S. & Ge, Z., 2016. Multiarray rupture imaging of the devastating 2015 Gorkha, Nepal, earthquake sequence, *Geophys. Res. Lett.,* **43**(2), 584–591.

SUPPORTING INFORMATION

Supplementary data are available at *GJI* online.

Figure S1. Backprojection results of the second source for the aftershock test. The procedure is the same as that applied to obtain Figs 4(e)–(h) in the manuscript, except that the waveforms of the first source are set to zero. The panel titles explain the backprojection methods. Contours represent the normalized radiation from

80:4:100, and crosses mark the peak-power locations of the backprojection images. Black lines in the seismograms mark the assumed occurrence times of the two sources, respectively (0 s and 15 s). The FDBP results are obtained using a $\Delta\omega$ range of 0.07–1.6 Hz.

Figure S2. Effects of depth phases in the backprojection images. The panel titles explain the backprojection methods. The red and blue stars represent the input locations of the first and second source, respectively. Black crosses mark the peak-power locations of the backprojection images for the two time windows (-7.5 to 7.5 s and 7.5 to 22.5 s). Orange lines in the synthetic seismograms mark the occurrence times of the two assumed sources (0 and 15 s), while dotted lines show the second time window. The FDBP results are obtained using a $\Delta\omega$ range of 0.07–0.2 Hz.

Figure S3. Backprojection results using swapped time corrections, that is low frequency time corrections applied to the high frequency band records and vice versa. Panels (a)–(d) low frequency backprojection results. Panels (e)–(h) high frequency backprojection results.